

Three-dimensional seismic structure of the Mid-Atlantic Ridge (35°N): Evidence for focused melt supply and lower crustal dike injection

Robert A. Dunn,¹ Vedran Lekić,² Robert S. Detrick,³ and Douglas R. Toomey⁴

Received 8 October 2004; revised 25 February 2005; accepted 24 March 2005; published 9 September 2005.

[1] We gathered seismic refraction and wide-angle reflection data from several active source experiments that occurred along the Mid-Atlantic Ridge near 35°N and constructed three-dimensional anisotropic tomographic images of the crust and upper mantle velocity structure and crustal thickness. The tomographic images reveal anomalously thick crust (8–9 km) and a low-velocity “bull’s-eye”, from 4 to 10 km depth, beneath the center of the ridge segment. The velocity anomaly is indicative of high temperatures and a small amount of melt (up to 5%) and likely represents the current magma plumbing system for melts ascending from the mantle. In addition, at the segment center, seismic anisotropy in the lower crust indicates that the crust is composed of partially molten dikes that are surrounded by regions of hot rock with little or no melt fraction. Our results indicate that mantle melts are focused at mantle depths to the segment center and that melt is delivered to the crust via dikes in the lower crust. Our results also indicate that the segment ends are colder, receive a reduced magma supply, and undergo significantly greater tectonic stretching than the segment center.

Citation: Dunn, R. A., V. Lekić, R. S. Detrick, and D. R. Toomey (2005), Three-dimensional seismic structure of the Mid-Atlantic Ridge (35°N): Evidence for focused melt supply and lower crustal dike injection, *J. Geophys. Res.*, *110*, B09101, doi:10.1029/2004JB003473.

1. Introduction

[2] Along slow spreading mid-ocean ridges the supply of melt from the mantle is viewed as spatially variable- and time-dependent [e.g., *Lin and Phipps Morgan*, 1992]. Consequently, such variations in melt flux are believed to control crustal thickness, lithospheric strength, and the partitioning of plate spreading between faulting and magmatism [e.g., *Cannat*, 1993, 1996; *Tucholke and Lin*, 1994; *Parsons et al.*, 2000]. For ridge segments bounded by tectonic offsets, the midsections tend to have the shallowest bathymetry and the thickest crust while the ends tend to exhibit deeper and wider axial valleys and thinner crust, as inferred from gravity data [*Kuo and Forsyth*, 1988; *Lin et al.*, 1990; *Detrick et al.*, 1995] and determined seismically [*Sinha and Loudon*, 1983; *Purdy and Detrick*, 1986; *Tolstoy et al.*, 1993; *Canales et al.*, 2000a; *Hooft et al.*, 2000; *Hosford et al.*, 2001]. Although these observations can be explained by several different mantle flow and melt flux

scenarios, each one predicts that melt flux is focused in the mantle and preferentially delivered to a segment’s center [e.g., *Whitehead et al.*, 1984; *Kuo and Forsyth*, 1988; *Lin et al.*, 1990; *Sparks et al.*, 1993; *Rabinowicz et al.*, 1993; *Magde et al.*, 1997]. By this view, there should exist a three-dimensional thermal structure in the newly forming lithosphere; at the segment midpoint the lithosphere should be thinner, hotter, and weaker than at the segment ends. Seafloor spreading should be more magmatically accommodated near a segment’s midsection and more tectonically accommodated at the ends [e.g., *Cannat*, 1993; *Tucholke and Lin*, 1994; *Gràcia et al.*, 1999; *Rabain et al.*, 2001]. In addition, the great diversity of ridge segment morphologies and variability in the maximum depth of seismicity [*Barclay et al.*, 2001], a proxy for lithospheric thickness, indicate that temporal variations in melt supply modulate this process: the diversity from segment to segment can be interpreted as reflecting various stages of a magmatic-tectonic evolution [e.g., *Cannat*, 1993; *Gràcia et al.*, 1999; *Barclay et al.*, 2001].

[3] This general model provides a valuable conceptual framework within which to understand slow spreading ridge morphology, crustal formation, volcanic activity, and tectonics. Verification of this model requires knowledge of the thermal structure and underlying magma supply of slow spreading ridge segments. Yet the three-dimensional (3-D) nature of the lower crust and uppermost mantle beneath any slow spreading ridge is poorly understood. As a step toward filling in this gap in knowledge, we compiled data from several wide-angle active source refraction experiments that

¹Department of Geology and Geophysics, School of Ocean and Earth Science and Technology, University of Hawai’i at Manoa, Honolulu, Hawaii, USA.

²Department of Earth and Planetary Science, University of California, Berkeley, California, USA.

³Department of Geology and Geophysics, Woods Hole Oceanographic Institution, Woods Hole, Massachusetts, USA.

⁴Department of Geological Sciences, University of Oregon, Eugene, Oregon, USA.

occurred along the Mid-Atlantic Ridge (MAR) near 35°N latitude and determined the first 3-D anisotropic image of both the crust and uppermost mantle of a slow spreading ridge segment. Our results provide new insight into the thermal structure and magma supply along a ridge segment and the partitioning of spreading between tectonic rifting and magmatism.

2. Mid-Atlantic Ridge at 35°N

[4] Our study area spans the northernmost of three ridge segments that are bounded by the Oceanographer (35°15'N) and Hayes (33°36'N) Fracture Zones (Figure 1). The northernmost segment, known as "OH-1" [Detrick *et al.*, 1995], is bounded to the south by a nontransform offset of the ridge near 34°32'N, which displaces the ridge axis in a right-lateral sense by 35 km. At its northern end the Oceanographer Fracture Zone displaces the ridge axis in a right-lateral sense by 110 km. The full spreading rate is estimated at ~22 mm/yr and the relative direction of spreading is at an azimuth of 100° from north [Le Douaran *et al.*, 1982; DeMets *et al.*, 1990]. OH-1 is 90 km long and exhibits an hourglass-shaped axial valley in map view, with a shallow, narrow midpoint and much deeper, wider ends. The segment's axial profile rises up from 4100 m depth at the fracture zone, to 2200 m depth at its midpoint. Continuing southward, it sinks again to 3300 m depth at NTO-1. The rift valley is nearly 40 km wide at its northern end, only 4–5 km wide at its midpoint, and up to 20 km wide at its southern end. The cross-axis relief at the segment midpoint is relatively low, only 300–400 m but is much greater at the segment ends, up to 3 km. A series of large volcanic cones, or seamounts, extends outward to either side of the ridge from the segment midpoint [Rabain *et al.*, 2001].

[5] Bathymetric and magnetic surveys show that OH-1 grew southward in length over the last 6 Ma [Rabain *et al.*, 2001]. The initiation of the propagation appears to have coincided with the initiation of the seamount chain. Large seamounts within the volcanic chain have the same magnetic polarity as the surrounding crust, indicating that they formed on the ridge axis and were subsequently rafted away from the ridge [Rabain *et al.*, 2001]. The first seamounts in the chain were located at the former southern boundary of the segment, suggesting that an increased magma supply in this area initiated the seamount chain and resulted in the southward propagation of the southern end of the ridge segment away from the new locus of enhanced magmatism. A prominent V-shaped scar in the seafloor bathymetry, which terminates at the nontransform offset, marks the path of propagation of the offset as it moved southward. Today, a large north trending ridge stands ~300 m above the valley floor and has a fault scarp associated with its eastern margin. The ridge is most prominent at the segment center, where it intersects the east-west seamount chain, and extends mainly northward. It also separates the main rift valley into a "western trough" and an eastern "axial valley" (often referred to as "the rift valley"); the western trough is relatively sedimented as compared to the eastern axial valley, which has little sediment cover and exhibits the most recent volcanism [Gràcia *et al.*, 1999]. From the bathymetric data it appears that at least two other low standing ridges extend northward from the segment's center

on the axial valley floor. One or more small ridges likewise appear to extend southward from the segment's center.

[6] Several lines of evidence indicate that more melt is currently delivered to the center of OH-1 than its ends. For example, the hourglass morphology and shallow water depth of the segment midpoint, an anomalously large mantle Bouguer gravity anomaly low centered on the segment, and the chain of seamounts that intersects the segment center have all been attributed to enhanced and focused mantle upwelling and magmatism near the segment center [Detrick *et al.*, 1995; Thibaud *et al.*, 1998; Rabain *et al.*, 2001]. Seismic studies indicate that a large component of the gravity low is due to a substantial thickening of the crust at the segment center [Sinha and Loudon, 1983; Hooft *et al.*, 2000; Canales *et al.*, 2000a; Hosford *et al.*, 2001]. Magde *et al.* [2000] seismically imaged, in three dimensions, a low-velocity zone at the segment midpoint that appears to extend downward into the lower crust. In addition, a two-dimensional refraction experiment located along the axial valley detected relatively low velocities at Moho (crust-mantle boundary) depths beneath the segment center [Hooft *et al.*, 2000]. A geologic survey [Gràcia *et al.*, 1999] found the axial valley floor at the segment center to be smooth, flat, and dominated by fresh sheet flows with no sediment cover and very few tectonic features (i.e., cracks, fissures, and faults), which mainly concentrate at the base of the central ridge's eastern flank. While the center of the segment appears to have a relatively high magmatic flux, the segment's ends appear to have undergone significant tectonic stretching. North and south of the segment center the sediment cover increases rapidly and tectonic features are more commonly observed.

[7] Several observations indicate that the upper 3–4 km of crust is cool and brittle. A seismic low-velocity layer observed throughout the top 1–2 km of the crust [Barclay *et al.*, 1998; Hooft *et al.*, 2000; Canales *et al.*, 2000a; Hosford *et al.*, 2001; Hussenoeder *et al.*, 2002], known as seismic layer 2, is observed here as well as worldwide in the oceans and is generally accepted to be the result of a high proportion of pores and cracks at these depths [e.g., Spudich and Orcutt, 1980; Detrick *et al.*, 1994; Swift *et al.*, 1998]. An analysis of the ratio of P to S wave velocity in the shallow crust and the detection of seismic anisotropy, an indicator of widespread ridge-parallel extension cracks, reveals that the upper 2 km of crust is pervaded with cracks and is thus relatively cool and brittle [Barclay *et al.*, 2001; Barclay and Toomey, 2003]. Microearthquakes recorded near the segment center indicate that the brittle-ductile transition is at four or more kilometers depth below the seafloor [Barclay *et al.*, 2001]. In summary, the upper 3–4 km of the crust at the segment center, and perhaps more so at the segment ends and in off-axis regions, is porous, permeable, and cool. There is no evidence for current high-temperature venting along this section of the MAR [Gràcia *et al.*, 1999], but low-temperature hydrothermal activity was found high on the eastern flank of the central ridge and a small hydrothermal plume anomaly was detected in the water column over the segment center [Chin *et al.*, 1998].

[8] The seismic structure of the upper crust is laterally variable and appears to reflect a variety of processes such as tectonic modification, crustal accretion variations, and

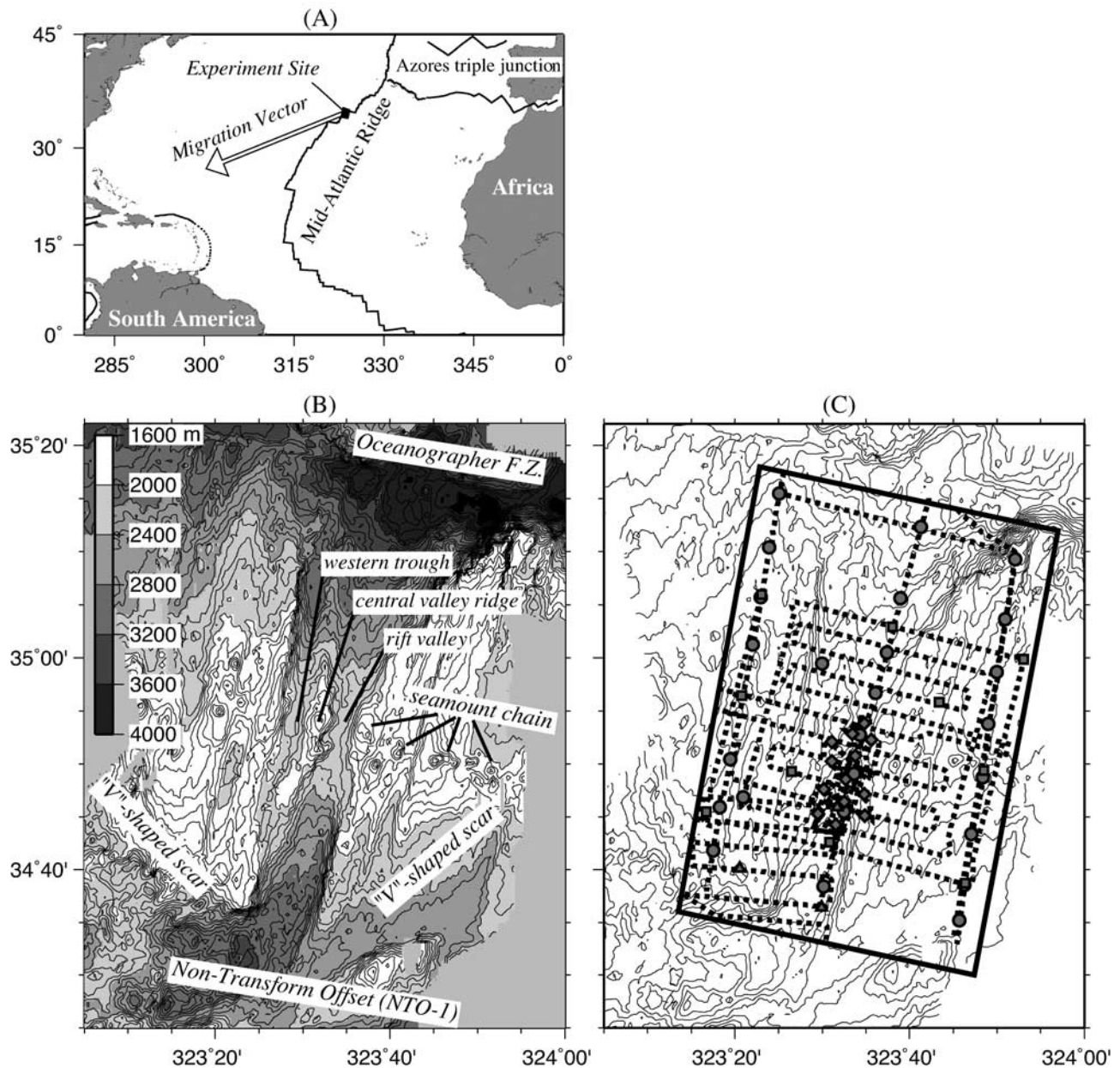


Figure 1. (a) Location of the seismic experiments along the Mid-Atlantic Ridge (35°N). Arrow indicates motion vector of the plate boundary in the hot spot reference frame. (b) Seafloor bathymetry (100 m contour interval) and major morphological features. (c) Layout of the seismic experiments superimposed on a contour map of the seafloor bathymetry (200 m contour interval). The study covers an $80 \times 55 \text{ km}^2$ region centered on the “OH-1” ridge segment. Symbols indicate locations of ocean bottom instruments: diamonds, the FARA experiment [Barclay *et al.*, 1998]; circles, the MARBE1 [Hooft *et al.*, 2000], MARBE3 [Canales *et al.*, 2000a], and MARBE4 [Hosford *et al.*, 2001] experiments; squares, MARBE5 [Magde *et al.*, 2000]; triangles, MARBE6 (previously unpublished). Our study consists of these 49 ocean bottom instruments and over 5000 air gun shots that occurred along the dotted lines.

crustal aging [Barclay *et al.*, 1998; Magde *et al.*, 2000; Hosford *et al.*, 2001; Hussenoeder *et al.*, 2002]. In contrast to fast spreading ridges where the axis of eruption is fairly narrow ($\sim 1\text{--}2 \text{ km}$), formation of new crust appears to occur over the entire width of the axial valley [Barclay *et al.*, 1998]. Crust produced near the segment ends lacks the usually distinct transition from seismic layer 2 to 3 and the upper crustal low-velocity layer is anomalously thick and low in velocity as compared to that near the segment center

[Sinha and Loudon, 1983; Canales *et al.*, 2000a; Hosford *et al.*, 2001]. Furthermore, the transition from crustal to mantle velocities appears to occur over a depth range of 3 km or more [Canales *et al.*, 2000a]. These seismic observations are consistent with a highly fractured and altered crust overlying a serpentinized upper mantle at the segment ends. This view is probably an over simplification, since serpentinites outcrop at the ends of some ridge segments [Gràcia *et al.*, 1997, 1999]. Several authors have suggested that the

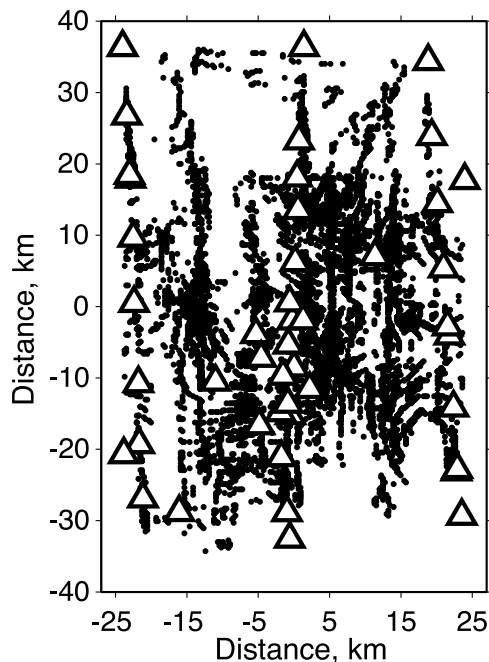


Figure 2. Ray penetration points (P_n) and bounce points (P_mP) on the Moho surface showing the distribution of information used to constrain the Moho depth. Triangles indicate station locations.

nontransform offset is a fundamental boundary of ridge magmatic segmentation [e.g., Canales *et al.*, 2000a; Kuo and Forsyth, 1988; Lin *et al.*, 1990].

3. Experiment and Data

[9] The target volume for the tomographic imaging is centered on the ridge segment, is approximately $80 \times 55 \text{ km}^2$ in area, and extends to 10 km depth beneath the seafloor (Figure 1c). The main portion of the data set was gathered in 1996 as part of the MARBE seismic tomography experiments [Hooft *et al.*, 2000; Canales *et al.*, 2000a; Hosford *et al.*, 2001; Magde *et al.*, 2000]. These experiments consisted of a 3-D tomography experiment with 11 ocean bottom instruments and 2700 airgun shots [Magde *et al.*, 2000] and three 2-D rise-parallel refraction experiments, one located along the rise [Hooft *et al.*, 2000] and the other two located 25 km to either side of the rise [Canales *et al.*, 2000a; Hosford *et al.*, 2001]; we use seven to eight instruments and ~ 300 air gun shots from each of the 2-D experiments. During shooting of the two off-axis refraction lines, lines of additional shots were carried out on the opposite sides of the ridge axis. Thus these instruments also recorded seismic energy that crossed the ridge axis. We also include three instruments and ~ 700 shots from a 3-D experiment that was partially located within the southwest quadrant of our area (previously unpublished). Almost all instruments recorded crustal P wave refraction arrivals (P), Moho reflections (P_mP), and mantle refractions (P_n). We include additional crustal refraction data (P) from a smaller 3-D tomography experiment, the FARA experiment [Barclay *et al.*, 1998], which was located near the ridge segment's center. Details of the shots and instruments, and

record sections of the data, appear in the respective papers, thus we do not repeat them here. Until this time, none of the P_mP and P_n data from 2-D shot-receiver geometries (i.e., shots and receivers not located along a single line) were included in any previous analysis. The data provide complete coverage of the crust and upper mantle over a $40 \times 50 \text{ km}^2$ area centered on the ridge, plus less complete coverage to the north and south. There are 360° of azimuthal ray coverage throughout the experiment's center, which is important for detecting anisotropy. Figure 2 displays a map view plot of ray penetration points (P_n) and bounce points (P_mP) on the Moho surface showing the distribution of information used to determine crustal thickness.

[10] Crustal P arrivals are clearly observed to distances of up to 20–40 km as first arrivals. Amplitudes of waveforms whose ray paths pass through the lower crust near the segment center are highly attenuated and the travel times are relatively delayed as compared to seismic energy that travels through the lower crust away from the segment center. The strength of the Moho triplication varies with spatial location, indicating variations in the nature of the transition from crustal velocities to mantle velocities. Stronger triplications indicate sharp velocity contrasts and a relatively thin Moho transition as compared to regions with a weaker triplication, which indicates a more gradual transition. In general, the transition appears to be relatively sharper at the segment center and more gradual to the north and especially to the south of the experiment center. Mantle P_n phases are observed for ranges of 25–60 km depending on station location and noise levels. Away from the experiment center, the slopes of P_n time-distance curves indicate mantle velocities of $\sim 7.8 \text{ km/s}$. P_n energy that passes through the experiment center has apparent velocities in the 7.3–7.5 km/s range for ridge-parallel paths and somewhat greater values for ridge-perpendicular paths, suggesting the presence of mantle anisotropy. In most cases the distinction between first arriving crustal P energy and first arriving P_n energy is clear and accompanied by a strong P_mP phase, although the P_n branch itself tends to have a low amplitude. Although we label the higher velocity energy as a mantle refraction, P_n , this energy could be turning either within unaltered mantle at the base of the crust, within a thick Moho transition zone, or at the base of a serpentinized region (such as might occur at the segment ends). However, the petrologic nature of the Moho transition is a question of interpretation and has no influence on the tomographic imaging process.

[11] The P - P_n crossover distance (distance between shot and receiver where P_n becomes a first arrival) is an indicator of crustal thickness; i.e., larger crossover distances indicate thicker crust. For energy that traversed the ridge to the north of the segment center, the crossover point occurs at $\sim 22 \text{ km}$ range (Figure 3). This is in contrast to energy that sampled the segment's center (both on and off axis), which exhibits crossover points at 40+ km range. South of the ridge segment's center, the distance is only 27 km. These general differences indicate thicker crust near the segment's center and the thinnest crust near the Oceanographer Fracture Zone.

[12] For imaging the crust and uppermost mantle in three dimensions, we compiled a data set of 31,405 P , 17,711 P_mP , and 11,716 P_n travel times from 49 ocean bottom

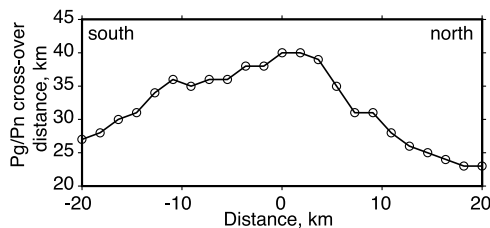


Figure 3. Plot of Pg/Pn crossover distances as a function of position along the ridge. The Pg/Pn crossover distance (distance between shot and receiver where Pn becomes a first arrival) is an indicator of crustal thickness; larger crossover distances indicate thicker crust. The crossover distance is determined from shot lines that are oriented perpendicular to the ridge axis and for receivers located along the westernmost and easternmost boundaries of the experiment. Thus the crossover distance roughly measures crustal thickness beneath the ridge. This plot indicates that the thickest crust resides at the ridge segment's center and thinner crust resides near the segment ends.

instruments. Where travel time picks were available from previous work, the picks were re-made to provide consistency in the picks and assigned uncertainties. The root-mean-square uncertainty is 24 ms for P , 47 ms for PmP , and 40 ms for Pn . The total combined data and experimental uncertainty is 37 ms. *Barclay et al.* [1998] explain the sources of experimental errors and their values for this type of experiment.

4. Methods

[13] Our seismic tomographic method is described in the Appendix. Grids for the velocity model and the Moho reflection surface are defined separately, but if the Moho is raised or lowered then the velocity values (not the velocity grid) change to maintain any velocity contrast associated with the interface. Model parameters for changes to isotropic slowness and the depth of the Moho are spaced 500 m and 1 km apart, respectively. Model parameters for anisotropy vary with depth only (unless otherwise noted), are spaced 500 m apart, and the fast axis of anisotropy is required to lie in a horizontal plane. Our method requires the user to set a priori uncertainties in the model slowness, interface depth, and anisotropy (σ_u , σ_z , σ_a) that act as damping terms to model perturbations (perturbations are changes to the starting model). Weighting values (λ_u , λ_z , λ_a) control the spatial smoothness of the image along with scale lengths of model smoothness (τ_x , τ_y , τ_z), which vary in depth with the width of the Fresnel zone, and are set to 500 m in the upper crust and increase to 2 km in the mantle. A tradeoff can exist between fitting travel time data with velocity perturbations versus Moho depth perturbations [e.g., *Ross*, 1994] and/or anisotropy perturbations [e.g., *Jousselin et al.*, 2003]. Since we perform a simultaneous inversion of the data, this permits a formal analysis of any such tradeoff. Although there is never a single solution to an inverse problem that contains real data with noise, with the large amount of data employed here the range of possible solutions is relatively small. Our goal was to construct smooth solutions, with the least

amount of variance that satisfies the data. Below we present one “standard” solution and then estimate its uncertainty by examining other solutions that fall within and outside the range of solutions that satisfy the data.

5. Results

[14] We first constructed a 1-D isotropic model (laterally invariant) from the results of *Magde et al.* [2000] for this area and added to it a Moho reflector at 5 km depth and a mantle layer of 7.8 km/s. We then inverted all of the data for a 1-D isotropic model that produces a minimum model misfit with the smoothest depth profile. The result (Figure 4) is a stable solution that removes the mean of the travel time delays (observed minus calculated times). The mean crustal thickness is ~ 6 km and the 1σ uncertainty of this mean is about 0.15 km, as estimated from the standard deviation of solutions determined by varying the ratio of σ_u to σ_z and by tests that forced the Moho to shallower and deeper depths.

[15] Using this 1-D solution as a starting model, we next solved for 3-D velocity structure and Moho topography. We performed a grid search over the values of σ_u , σ_a , σ_z , λ_u , λ_a , and λ_z to determine the range of values that produce viable solutions. To reduce the complexity of this search, we first performed the grid search for isotropic solutions and then once a suitable range of models was identified, we added and varied the anisotropic parameters. Values of $\sigma_u \geq 0.08$, $\sigma_a \geq 0.005$, and $\sigma_z \geq 0.75$ provided enough model variance to produce viable fits to the data if the smoothing weights were not too large ($\lambda_u \leq 175$, $\lambda_a \leq 1000$, and $\lambda_z \leq 50$). Figure 5 shows the solution most representative of those that provide the best statistical fit to the data. The parameter values for this “standard solution” are $\sigma_u = 0.10$, $\sigma_a = 0.015$, $\sigma_z = 1$, $\lambda_u = 150$, $\lambda_a = 1000$, $\lambda_z = 30$. We chose this solution by first averaging solutions that fit the data ($1 <$

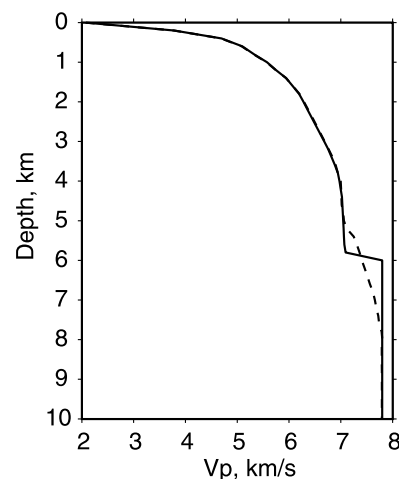


Figure 4. Plot of P wave velocity versus depth below the seafloor. The 1-D velocity solution is shown by dashed line. Because of crustal thickness variations, the 1-D solution averages the Moho transition zone over a range of depths. Thus we modified the velocity profile to create a starting model for the 3-D inversions (solid line) that has a single step from crustal to mantle velocities at the average depth of the Moho reflector.

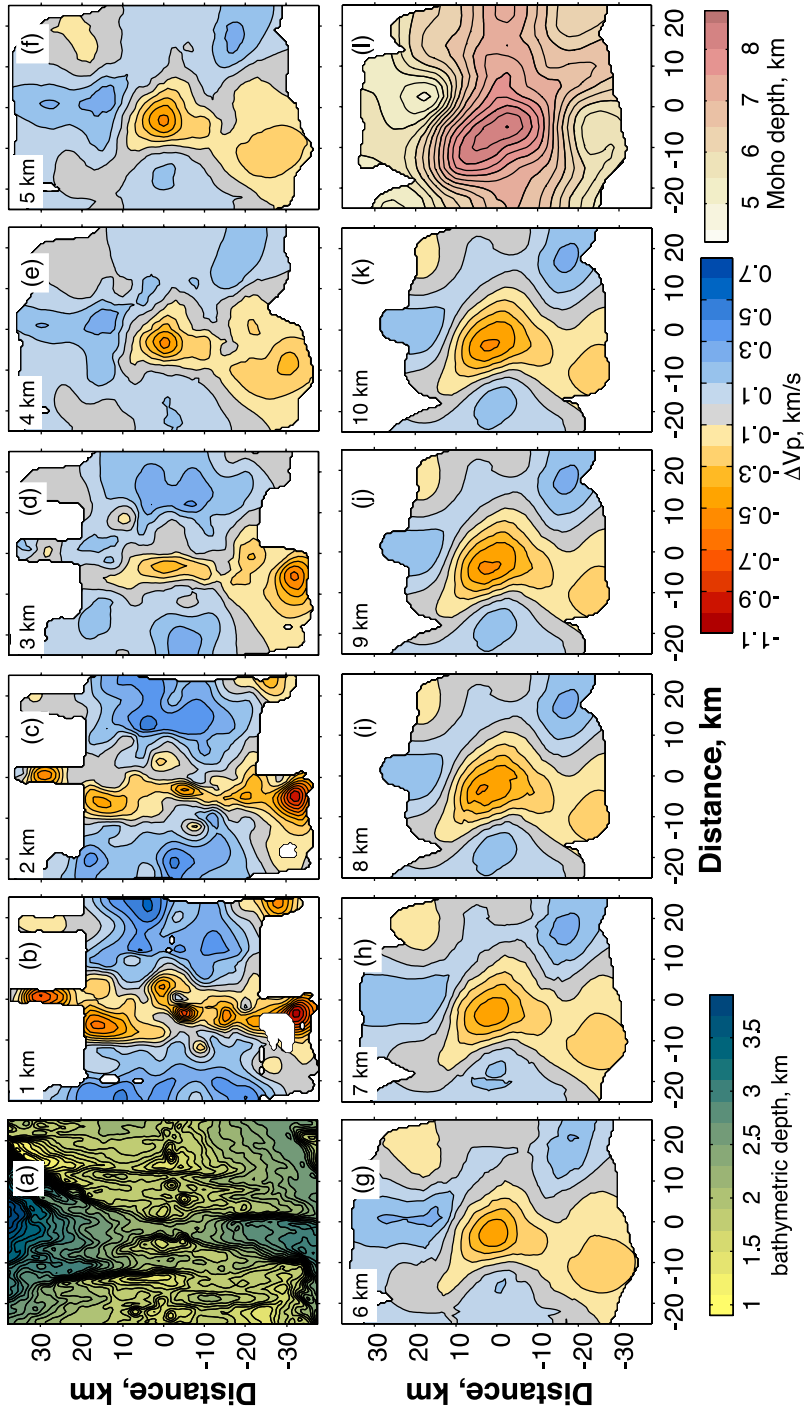


Figure 5. Three-dimensional anisotropic tomographic solution; this is our “standard” solution for comparison to other solutions. (a) Bathymetric map of the area with 100 m contour interval. (b)–(k) Map view sections of the 3-D velocity perturbations relative to the starting 1-D model shown in Figure 4. The depth of each section is indicated. The contour interval is 0.1 km/s. (l) Crustal thickness map with a 250 m contour interval.

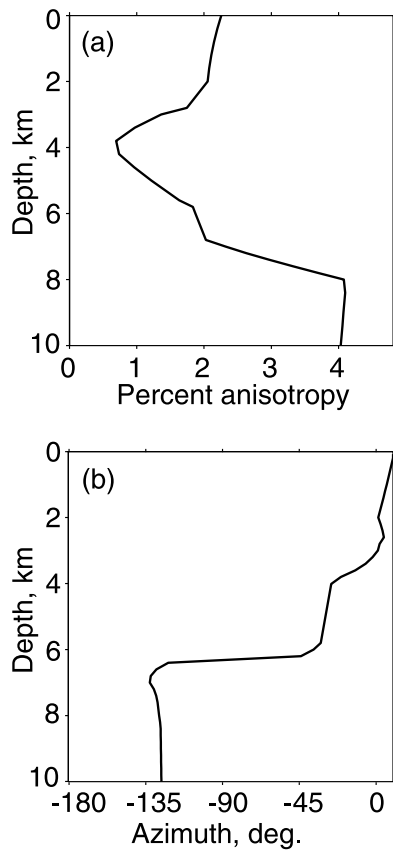


Figure 6. (a) Percent anisotropy and (b) azimuth of the fast axis as a function of depth for the standard solution shown in Figure 5. Zero degrees azimuth is along the ridge axis in the northward direction.

$\chi^2 < 1.1$) and then selecting the solution that most closely resembled the average.

[16] The standard model has the following key characteristics. The crust is thickest at the segment center, thins rapidly northward and less rapidly southward. The mantle contains a strong low-velocity “bull’s-eye” anomaly at the segment center. This anomaly continues up into the crust and is reduced in both size and amplitude as it approaches the upper crust. In the uppermost crust, velocities are generally low in a broad band that extends along the ridge axis from north to south. The shallow velocity structure is also strongly heterogeneous with many small (<10 km width) negative anomalies and more subdued positive anomalies. Two percent anisotropy, with the fast direction of energy propagation parallel to the ridge, is detected at shallow crustal levels (Figure 6) and 1–2% anisotropy is detected in the lower crust. Mantle anisotropy is 4% with the fast direction at an azimuth of $\sim 38^\circ$ counterclockwise from the ridge-perpendicular direction. Our images of the upper crust are similar to those of *Magde et al.* [2000], but show more detail due to the larger data set employed here.

5.1. Changes to σ_u and σ_z

[17] Figure 7a shows the misfit as a function of σ_u and σ_z . The set of solutions that fit the data ($1 < \chi^2 < 1.1$) vary by ≤ 0.1 km/s in velocity and < 150 m in Moho topography and are thus essentially the same. For fixed smoothness values

and within the range of acceptable misfits, changes to the a priori solution variance result in insignificant trade-off between velocity structure and crustal thickness. Instead, the small variation in structure that is allowed by the data is almost exclusively controlled by the smoothness parameters (see below). An example of an alternative solution that provides a statistically similar misfit as compared with the standard solution (see Figure 7a), but with much different σ_u ($= 0.075$) and σ_z ($= 3$), is shown in Figures 8a–8d; as one can see, this solution and the standard are equivalent. In general, increasing σ_u or σ_z , with all other adjustable parameters set to the “standard” values, has the primary effect of allowing velocity perturbations to “bleed” into areas of insufficient ray coverage (areas masked out in

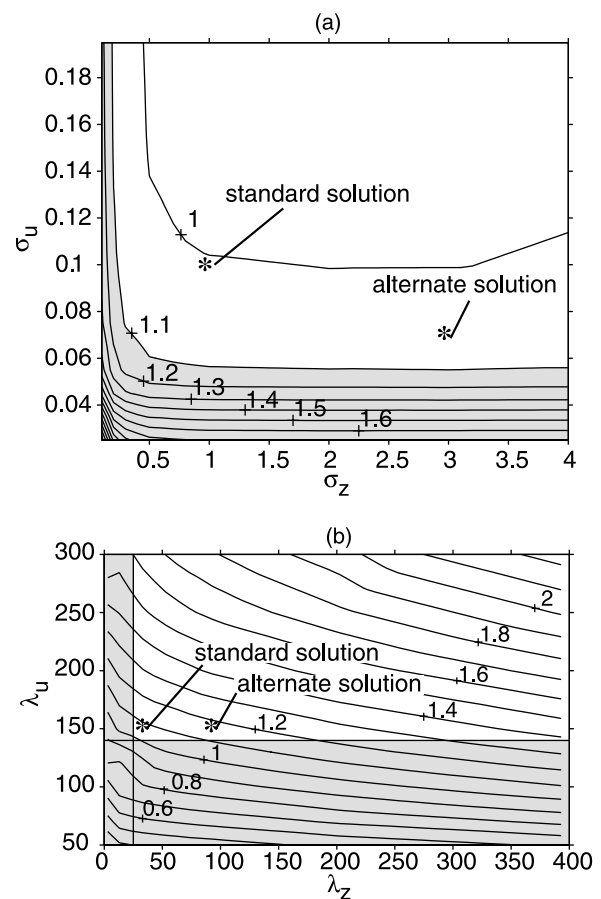


Figure 7. (a) Contour plot of the χ^2 misfit obtained by varying σ_u and σ_z . Smoothing values are fixed at $\lambda_u = 150$, $\lambda_a = 1000$, and $\lambda_z = 30$. We reject solutions that lie in the gray shaded area since they are too heavily damped (do not contain enough structure) to satisfy the data. (b) Contour plot of the χ^2 misfit obtained by varying λ_u and λ_z . In this case, we reject solutions that lie in the gray shaded areas since they are too rough to be resolved by the data and are clearly corrupted by data noise. Furthermore, solutions with misfits > 1.1 can be rejected since they are too smooth and do not provide a good fit to the data (as determined by an F test at the 95% confidence level). Thus the range of acceptable models is quite small. The parameter values for the alternative solutions shown in Figures 8a–8d and Figures 8e–8h are indicated in Figures 7a and 7b, respectively.

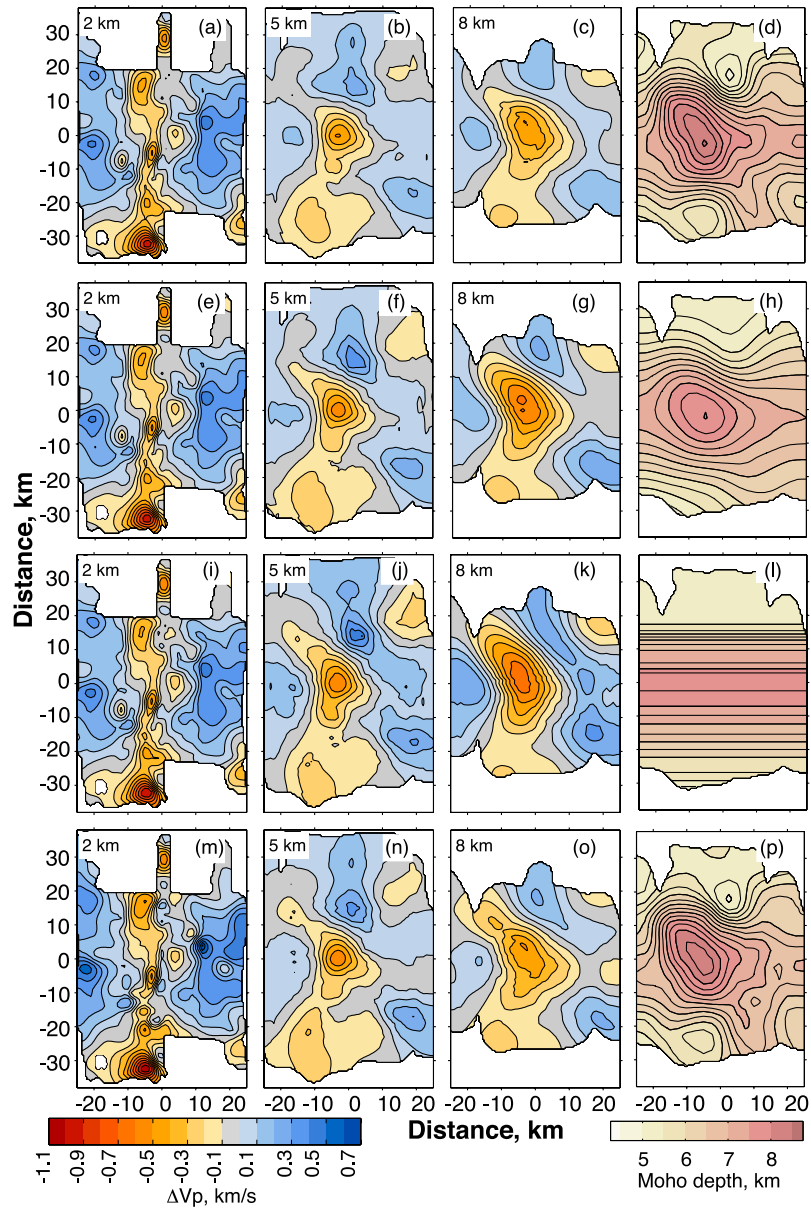


Figure 8. Four alternative tomographic solutions to test the uniqueness of our standard solution. The first three columns are depth slices through each solution; the depth is indicated. The fourth column is the crustal thickness map for the solution. (a and b) Similar to the standard model shown in Figure 5 except $\sigma_u = 0.075$ and $\sigma_z = 3$. (e–h) Similar to the standard model except $\lambda_z = 90$. (j–l) Similar to the standard model except that the crustal thickness was restricted to vary only along the ridge. (m–p) Similar to the standard model except that no anisotropy was allowed.

Figures 5 and 8). Reducing σ_u (or σ_z) raises the χ^2 misfit rapidly by reducing the magnitude of velocity (or Moho) variations without changing their form; we reject such solutions based on their poor fits to the data. For any set of smoothing weights, no solutions with only lower-crustal velocity ($\chi_{PmP}^2 > 3.5$) or only Moho topography variations ($\chi_{PmP}^2 > 5$) fit the *PmP* data.

5.2. Changes to λ_u and λ_z

[18] Figure 7b shows the misfit as a function of λ_u and λ_z . Smooth and heavily damped solutions fit the data poorly. On the other hand, the roughest solutions (gray shaded areas in Figure 7b) exhibit velocity structure that is too rough to

be constrained by the data, on the basis of the Fresnel zone of the seismic waves and checkerboard resolution tests (Figure 9), and are clearly corrupted by data noise. Models that best fit the data, $1 < \chi^2 < 1.1$, occur over a small set of smoothness values and are very similar in appearance. An example of an alternative solution that has almost the same data misfit (an *F* test at the 95% confidence level indicates that the standard solution does provide a better fit to the data than this alternate solution) is shown in Figures 8e–8h; this solution has the same parameterization as for the standard solution except $\lambda_z = 90$, or triple the standard value. While the mantle velocity anomaly is increased by ~ 0.1 km/s in magnitude, the Moho topography is smoother across the

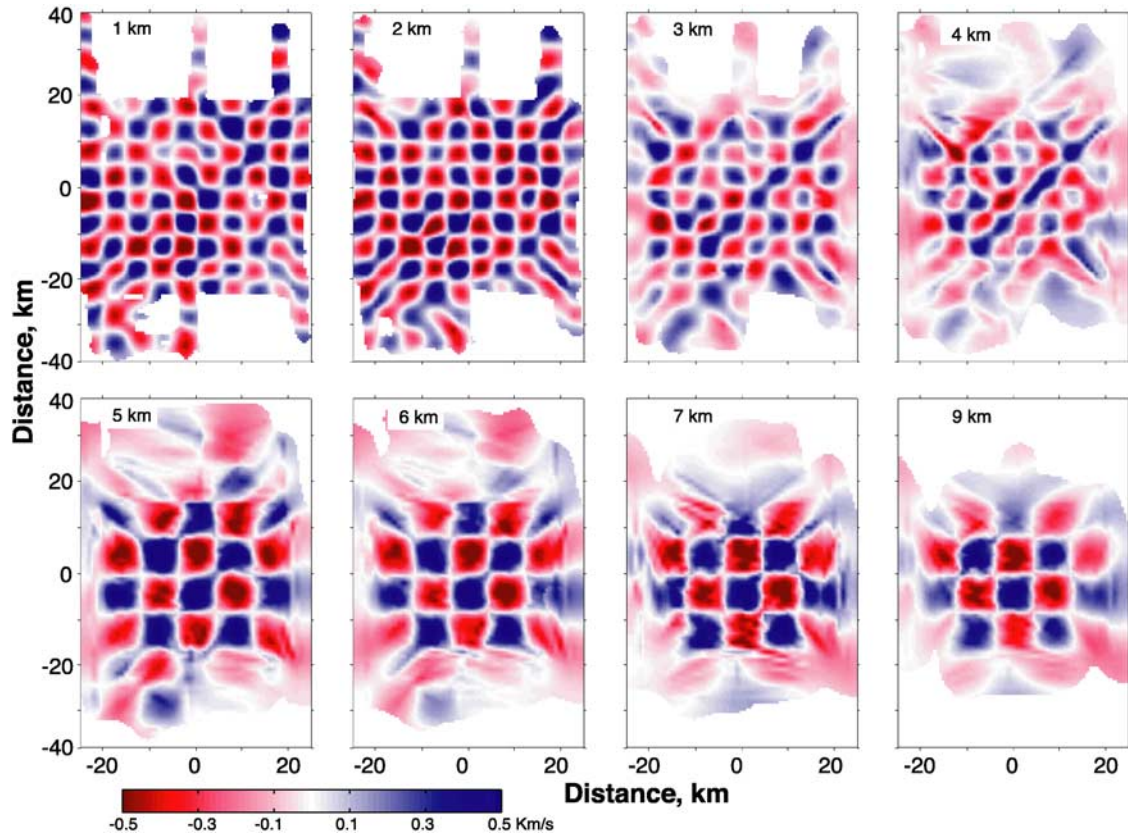


Figure 9. Model resolution is estimated via the reconstruction of “checkerboard” models. Travel times are computed for checkerboard models using a fixed ray set (rays calculated with respect to the standard solution of Figure 5) and Gaussian noise with a 30 ms standard deviation added. The synthetic data are then inverted using the same parameterization as for the standard solution. Small block sizes of 2–3 km width are resolvable in the central portion of the experiment; far from the experiment center, only larger block sizes are resolvable. Here we show example reconstructions at different depths (depth of each image is indicated); bear in mind that smaller block sizes are also resolvable near the experiment center and that areas showing no resolution in these images have resolvable structure for larger block sizes. The high resolution at the experiment center results from the excellent azimuthal, horizontal, and vertical distribution of rays that pass through this region.

ridge with the maximum crustal thickness reduced by ~ 0.5 km. In general, for fixed model uncertainties and within the range of models that fit the data, velocities vary by ≤ 0.1 km/s and crustal thickness varies by < 0.5 km. If we allow only ridge parallel or ridge perpendicular variations in the velocity structure of the upper crust, lower crust, or mantle, it is not possible to find a model that satisfies the data and we conclude that 3-D variations in velocity structure are required at all depths. In addition, ridge-parallel variation in Moho topography is also required by the data. We tested whether the data requires ridge-perpendicular variations in Moho topography (Figures 8i–8l) and found that solutions with ridge-perpendicular variations of ± 0.5 km, such as for the standard model, do provide a statistically better data misfit. Larger variations are not required by the data, but reduced variations of ± 0.4 km provide a statistically similar misfit.

[19] In summary, we find that the trade-off between velocity structure and Moho topography is small. For the class of solutions that satisfy the data the overall form of the velocity structure and Moho topography is not significantly different from one solution to the next. However, small-

scale features do change form, suggesting caution when interpreting such features in the solutions. While the range of acceptable solutions is small, a solution still depends on the resolution inherent in the experiment geometry and parameterization. Thus we must always examine other indicators of resolution, such as the checkerboard resolution figures in Figure 9.

5.3. Isotropy Versus Anisotropy

[20] Figures 8m–8p show an isotropic solution ($\chi^2 = 1.4$) that was otherwise constructed in the same manner as for the standard solution. Travel time residuals for this solution reveal a $\cos(2\theta)$ pattern, where θ is the ray path azimuth (Figure 10). This residual pattern is indicative of anisotropy where the wave speed varies as a function of azimuth. Because of the dense ray coverage and excellent azimuthal coverage, the anisotropy signal ends up in the data residuals of the isotropic solution and is only insignificantly mapped into isotropic structure. Solving for depth-varying anisotropy as part of the inversion removes the $\cos(2\theta)$ trend in the residuals and reduces the data misfit. As the amount of anisotropy is allowed to increase, by varying σ_u/σ_a , the

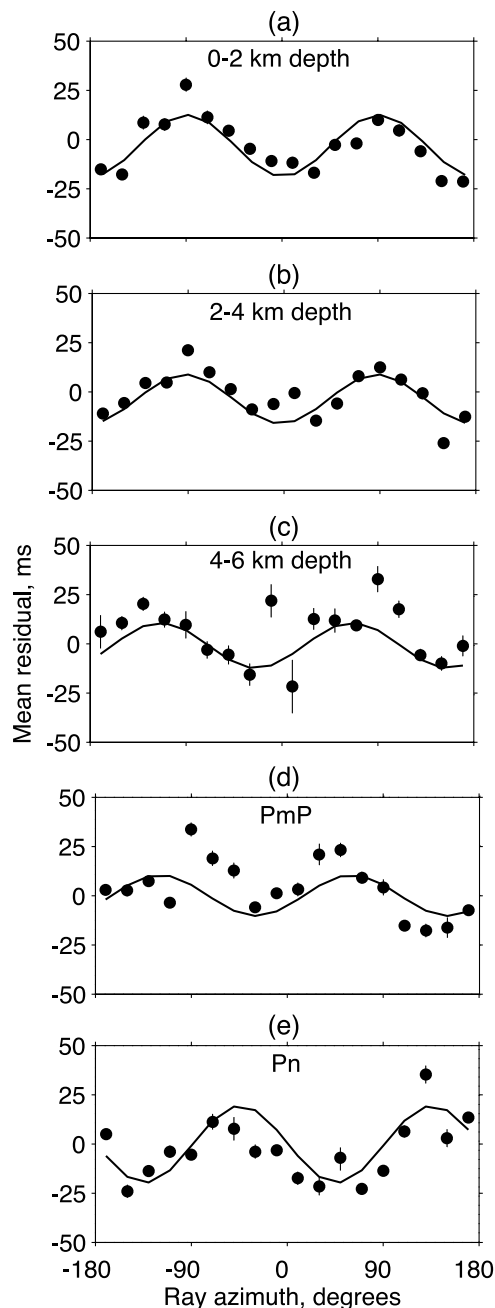


Figure 10. Travel time residuals (observed minus calculated times) for the isotropic solution (Figures 8m–8p). The residuals are sorted into 20° bins by a ray path’s azimuth, and the mean of each bin is plotted along with the 1σ standard deviation of the mean. Residuals for crustal refracted rays whose maximum depths lie between (a) 0–2 km depth below the seafloor, (b) 2–4 km depth, and (c) >4 km depth exhibit clear anisotropic signals via a $\cos(2\theta)$ variation, where θ is ray azimuth. (d) *PmP* rays exhibiting a $\cos(2\theta)$ pattern. (e) Mantle refractions exhibiting a $\cos(2\theta)$ pattern but with the fast axis in a southwest/northeast direction.

residual $\cos(2\theta)$ patterns decrease in amplitude and then disappear at $2.5 \pm 0.5\%$ anisotropy in the upper crust, $2 \pm 0.5\%$ in the lower crust, and $4 \pm 0.5\%$ in the mantle. The azimuth of the fast direction changes little with changes in

the ratio σ_u/σ_a , and is independent of the starting value. Allowing fully 3-D variations in anisotropy did not improve the data misfit and the results were heavily influenced by the azimuthal distribution of ray paths throughout the model.

6. Examination and Interpretation of the Tomographic Images

6.1. Shallow Crust

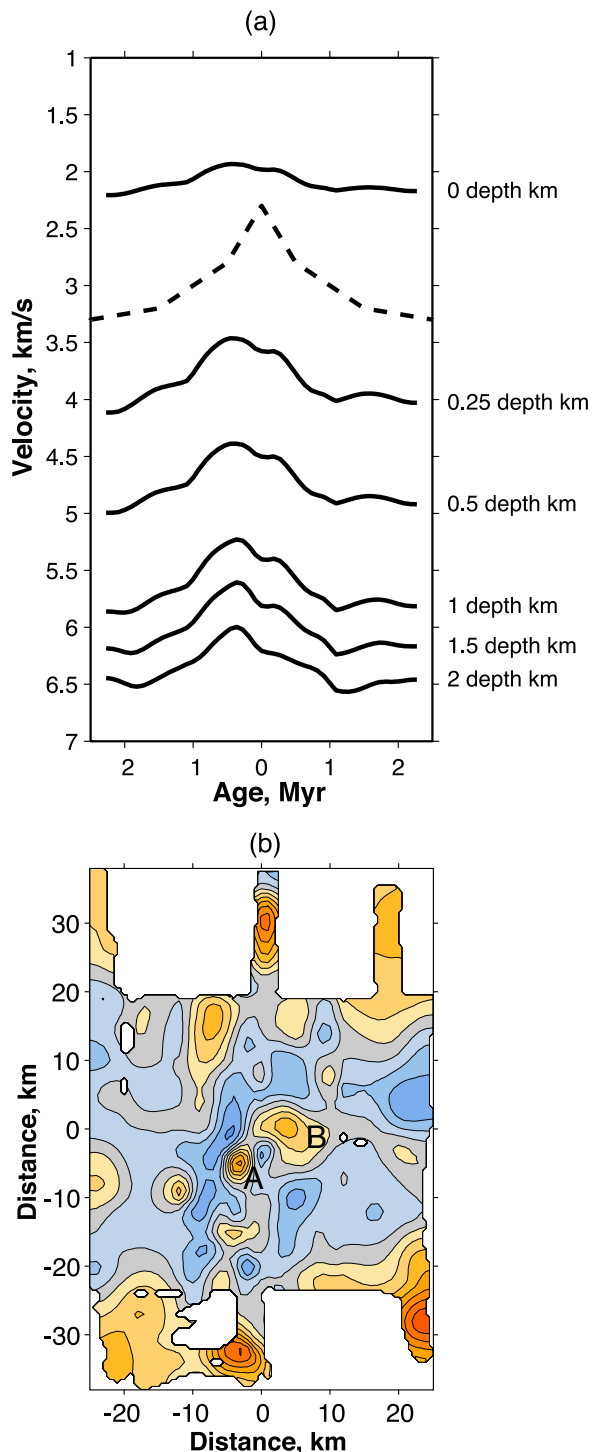
[21] As summarized in section 2, there are now several observations suggesting that the upper 2–3 km of crust is relatively cool, brittle, porous, and riddled with cracks. Our average 1-D isotropic structure (Figure 4) reveals low velocities in the shallow crust that are also indicative of high degrees of porosity. In addition, the upper crustal anisotropy is consistent with vertically oriented, ridge-parallel cracks that are the result of extensional stresses. The increase in velocity and decrease in anisotropy with depth can be attributed to the reduction in crack/pore volume with depth, via a combination of closing of cracks and pores with increasing pressure and a decrease in the vesicularity of lithologic units [e.g., *Swift et al.*, 1998]. In three dimensions (Figure 5), upper crustal velocities are anomalously low in a broad axial band that parallels the ridge axis. Relatively low on-axis velocities with respect to higher off-axis velocities are a global phenomenon and widely interpreted to reflect a porous upper crust near the ridge axis that subsequently decreases in porosity, and hence increases in velocity, with crustal age due to infilling of cracks and pores via hydrothermal deposition [e.g., *Houtz and Ewing*, 1976; *Purdy*, 1987; *Grevemeyer and Weigel*, 1997]. Figure 11a compares the global average trend in layer 2A velocities of *Grevemeyer and Weigel* [1997] to our results in the 0–2 km depth range (averaged along the ridge). Although tomography experiments provide poor constraints on layer 2A velocities, the global average falls within our range of upper crustal velocities. Importantly, the ridge-perpendicular variation that we find in the shallow crust (<0.75 km/s) can be largely explained by crustal aging.

[22] After subtracting the local average velocity profile, small-scattered anomalies and extensive low-velocity regions near the transform and nontransform offsets remain (Figure 11b). These variations can arise from lateral variations in pores, cracks, alteration products, and the ratio of porous extrusive rocks to less porous intrusive rocks, and likely reflect the nonuniform construction of the upper crust with time. At the segment ends, we interpret the extensive low-velocity regions located both on and off axis as the result of a greater percentage of cracks due to greater tectonic stretching. In support of this interpretation, geologic mapping of the seafloor [*Gràcia et al.*, 1999] reveals greater densities of cracks and fissures at the segment ends than the segment center. Two negative anomalies near the segment center, labeled “A” and “B” in Figure 11b, underlie volcanic cones and by association may be due to locally higher-than-average temperatures (hundreds of degrees) as suggested by *Magde et al* [2000]. Detection of high-temperature hydrothermal venting at these seamounts would support this interpretation, yet few measurements have been made to date and there is only evidence for fossil hydrothermal sites and low-temperature diffuse flow on the eastern side of the central ridge near “A” [*Gràcia et al.*, 1999] and a small water column

plume near the segment center in general [Chin *et al.*, 1998]. Alternatively, the anomalously low velocities associated with these seamounts could be explained by very thick, low-velocity extrusives associated with seamount volcanism.

6.2. Middle to Lower Crust and Mantle

[23] Velocities near the segment ends are roughly similar to off-axis velocities, indicating similar temperatures. However, velocities are higher at the northern end of the ridge segment than at the southern end, indicating $\sim 300\text{--}550^\circ$ cooler temperatures.



[24] At the center of the segment, if we assume that the brittle-ductile transition is near 4 km depth, as indicated by the microearthquake study of Barclay *et al.* [2001], then the large low-velocity zone is most likely due to elevated temperatures and a small amount of melt at depths >5 km (Figures 5e–5k). It is difficult to predict absolute temperatures or melt fractions due to a lack of baseline temperature information away from the ridge. Nevertheless, if we first assume that the low-velocity anomaly is due to temperature only, then at the base of the crust the corresponding thermal anomaly is $\sim 500\text{--}900^\circ$ (applying the methods described by Dunn *et al.* [2000, and the references therein]. Therefore, if the temperature at the Moho is $\sim 800^\circ\text{C}$ at a point 15–20 km away from the ridge axis [Phipps Morgan and Chen, 1993], then the calculated temperature beneath the ridge, $1300\text{--}1700^\circ\text{C}$, exceeds expected liquidus temperatures of the lower crust [e.g., Sinton and Detrick, 1992]. This is illogical since the assumption of no melt results in a prediction of a fully molten lower crust. Consequently, a portion of the low-velocity anomaly is likely due to a small amount of melt. Assuming that the thermal anomaly is $200\text{--}300^\circ$ requires 3% melt distributed over a 10×10 km² area beneath the segment midpoint to account for the additional reduction in velocity. Tomographic methods tend to underpredict the magnitude of low-velocity zones; thus 3% is a minimum value. Given that the resolution of the imaging is no better than $\sim 3\text{--}4$ km near the Moho, the melt could exist along grain boundary interfaces or within larger isolated regions with higher melt concentrations, which when averaged together make up the 3% melt fraction. For example, the lower crust could be composed of partially molten dikes and sills.

[25] The presence of anisotropy in the lower crust is unexpected, but could be produced by partially molten magmatic dikes. To test whether this anisotropy is mainly present beneath the hot central portion of the ridge, and is thus due to dikes, or is mainly present at the colder segment ends and off-axis areas, and is thus due to fracturing or faulting, we examined travel time residuals from the isotropic solution (Figures 8m–8p). We gathered lower crustal *P* refractions and all *PmP* rays and then subdivided these residuals into one group where the turning points of the rays were located within the large low-velocity zone at the center of the segment and another group where the turning points were located outside of this region. Travel times are most sensitive to anisotropy at the rays' turning depth. Rays

Figure 11. (a) Ridge-perpendicular profiles of velocity as a function of predicted crustal age (solid lines). Each profile is the average of the velocity structure, taken along the ridge, at the specified depth. Ages are computed from distance divided by half spreading rate. The seafloor profile is poorly constrained because ray paths that travel through the uppermost crust are nearly vertical. Dashed line: Global average variation in layer 2A velocities [Grevemeyer and Weigel, 1997]. (b) Crustal velocity structure at 1 km depth from Figure 5 but with the age-related trend removed. Velocities are anomalously low near the ridge offsets and beneath at least two seamounts (labeled A and B) near the ridge segment's center. Color scale is the same as for Figure 5.

whose turning points are located in the low-velocity zone exhibit the $\cos(2\theta)$ pattern, while rays that turn outside this region do not. Thus we conclude that the lower crustal anisotropy arises from elastic anisotropy within the large low-velocity region in the center of the ridge segment, and we suggest that this anisotropy is due to vertical dikes in the lower crust that are roughly oriented along a line that is rotated $30\text{--}40^\circ$ counterclockwise from the ridge axis.

[26] Two percent anisotropy can be generated by 6% melt fraction in dikes that make up 50% of the lower crust or 50% melt fraction in dikes that make up 6% of the crust. In either case, these numbers agree with the 3% average melt fraction determined from the isotropic reduction in velocity alone. This result was determined by assuming the host rock is 6.8 km/s with a Poisson's ratio of 0.28 and density

2800 kg/m^3 ; the dikes are assumed to have a Poisson's ratio of 0.28 and a velocity given by that of the host rock minus the effect of the melt, which is determined by $\partial \ln V_p / \partial \phi = 3$ [Schmelting, 1985], where ϕ is melt fraction. The percentage anisotropy is determined by weighted averages of the elastic parameters, where the weights are determined by the fraction of crust composed of dikes and that of host rock [Auld, 1973; Schoenberg, 1983]. The effects of Poisson's ratio and density are small on these calculations.

[27] Mantle anisotropy is 4% with the azimuth of the fast axis oriented in a southwest direction at $\sim 38^\circ$ from the ridge-perpendicular direction or 250° from north. At 35°N , an estimate of the velocity vector of ridge motion over the mantle in a hot spot reference frame can be found from the HS3-NUVEL-1A plate motion model [Gripp and Gordon, 2002] and the methods of Stein *et al.* [1977]. Assuming symmetric spreading [Le Douaran *et al.*, 1982; Rabain *et al.*, 2001], a point on the ridge axis moves in a direction roughly 248° from north (Figure 1a) at a rate of 3 cm/yr, or at almost three times the half spreading rate. Thus, on both sides of the ridge the half rate spreading vector plus the migration vector results in a vector that points to the southwest. Assuming that the fast direction of seismic anisotropy points in the direction of mantle flow, we conclude that mantle flow just beneath the ridge is dominated by ridge migration in the hot spot reference frame and not by relative plate motion.

6.3. Crustal Thickness

[28] Our 2-D crustal thickness map (Figure 5l) shows good agreement with previous crustal thickness profiles for this area [Canales *et al.*, 2000a; Hooft *et al.*, 2000; Hosford *et al.*, 2001]. Together, these studies reveal 8.5 ± 0.5 km thick crust near the segment center and 4–5 km thick crust to the north and south of center. Note that Hooft *et al.* [2000] detected even thinner crust (3–4 km thick) outside of our experiment area near the Oceanographer Fracture Zone. Our study reveals that ridge-perpendicular variations in crustal thickness are modest, $\leq \pm 0.5$ km. There are small differences between the different studies that can be attributed to the trade-off between crustal velocity values and Moho depth. For example, the Moho depths reported by Hosford *et al.* [2001] tend to be deeper and show less along-

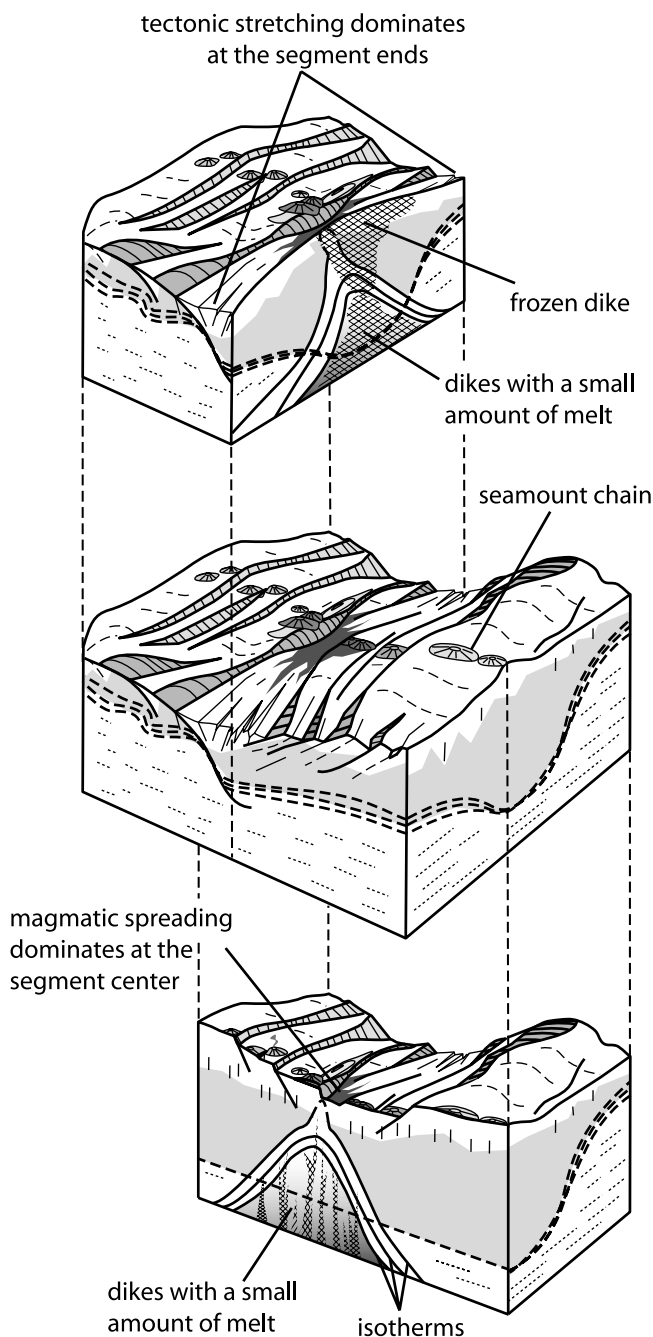


Figure 12. Cartoon summary of our principal results and interpretation of the magmatic and tectonic processes along this ridge segment. We suggest that melts ascending from the mantle are focused toward the center of the ridge segment at subcrustal depths and subsequently penetrate the crust through a cluster of dikes. This process creates thicker crust at the segment center and a weaker lithosphere. Consequently, plate spreading is accommodated more by magmatism than by tectonism at the segment center; the reverse is true at the segment ends. Scattered velocity anomalies and nonuniform aging of the shallow crust indicate that formation of the shallow crust is unstable over time, revealing a strong interplay between magmatism, tectonism, and hydrothermal circulation. In contrast, the uniformity of the crust's thickness as a function of age indicates that the time-averaged melt flux to the ridge is relatively uniform.

axis variation. Given the limited data coverage in that analysis there is probably a larger velocity-depth trade-off than in our study and the high crustal velocities just above the Moho in their study (7.2–7.6 km/s) probably compensate for the reflector being too deep.

7. Discussion

[29] The OH-1 ridge segment is a single accretionary unit of crustal formation at a slow spreading ridge. Our results, along with those of previous studies, provide a consistent view of the melt supply to this ridge segment and the partitioning of plate spreading between magmatism and faulting (Figure 12). Our results indicate that mantle-derived melts rising beneath this ridge segment are preferentially focused at mantle depths toward the center of the segment, resulting in both thicker crust at the segment center and a region of high temperatures and melt within the uppermost mantle and lower crust. We suggest that magma intrudes into a hot, subsolidus, lower crust within dikes. The trend of the dikes, which is given by the fast axis of anisotropy is not perpendicular to the relative spreading direction, but is rotated $\sim 30\text{--}40^\circ$ from the ridge-parallel direction. This rotation may be related in some way to stresses generated by the $\sim 40^\circ$ difference between the absolute motion of the spreading center and the relative spreading direction.

[30] The lack of evidence for a magma supply at the segment ends suggests that crust is formed at the ends via melt that is fed out along the ridge at crustal levels from the central source region, in a manner similar to Hawaiian-type rift zones as suggested by *Smith and Cann* [1999]. *Abelson et al.* [2001] found evidence for magma flow in crustal dikes in the Troodos ophiolite, which is believed to be a section of oceanic crust that formed in a slow spreading environment. Their measurements of the anisotropy of magnetic susceptibility reveal anisotropic fabric of the gabbroic section of the ophiolite and indicate ridge-parallel flow lines aligned from the center of the ridge segment to its termination at a fossil transform. On the other hand, along OH-1 perhaps not all melts that form the crust at the segment ends pass through the segment center. Geochemical sampling of the OH-1 ridge axis by *Niu et al.* [2001] reveals a peak in apparent enrichment of incompatible elements near the segment center. They argue that their data requires a heterogeneous mantle source beneath this segment. If true, and all melts pass through the segment center, then one would expect to see enriched basalts everywhere along the ridge. Since this is not observed, either the heterogeneous mantle model is incorrect, or much of the melt that forms crust at the segment ends comes from directly below those regions. A test of these ideas and models of mantle flow and melt supply in general requires additional isotope studies and deeper mantle seismic and electromagnetic imaging.

[31] The data do not require large crustal thickness variations in the direction parallel to spreading, although smaller $\leq \pm 0.5$ km variations are required by the data and we conclude that the OH-1 segment has received a relatively continuous melt supply over the last 2.5 Myr and perhaps as long as 6 Myr [*Rabain et al.*, 2001]. This is in sharp contrast to the $23^\circ 20' \text{N}$ region of the MAR (MARK area), which exhibits strong crustal thickness

undulations in the spreading direction [*Canales et al.*, 2000b]. It is possible that OH-1 is anomalous in this respect; its proximity to the Azores hot spot may result in a more continuous melt supply than for other slow spreading sections of ridge.

[32] Our results show that there exists a 3-D thermal structure in the newly forming crust; at the segment midpoint the lithosphere is thinner and the crust hotter than at the segment ends. Thus a thin hot lithosphere and a greater magma supply (as indicated by the thicker crust) result in a greater degree of magmatically controlled spreading. The segment ends, in contrast, undergo significant tectonic stretching. In the upper crust where seismic velocities are largely controlled by chemical alteration, porosity, and crack density, our tomographic images, along with previous work [*Hoofft et al.*, 2000; *Canales et al.*, 2000a; *Hosford et al.*, 2001], indicate that the segment ends are heavily fractured and altered. In the lower crust and mantle where velocities are mainly controlled by temperature and melt, our tomographic images indicate that the segment ends are relatively cool, with a thick lithosphere. Higher velocities near the Oceanographer transform than near the nontransform offset indicate a greater degree of deep cooling due to sustained, deep pathways for hydrothermal circulation. Several other observations suggest colder lithosphere at the segment ends with greater tectonic extension and low magma supply; for example, the deep and wide axial valley with a cross-axis relief $\sim 6\text{--}10$ times that of the segment midpoint [e.g., *Rabain et al.*, 2001], the faulted and sedimented seafloor [*Gràcia et al.*, 1999], and the lack of hydrothermal output [*Chin et al.*, 1998; *Gràcia et al.*, 1999].

8. Conclusions

[33] 1. A large low-velocity “bull’s-eye” is imaged beneath the center of the ridge segment from 4–10 km depth. The velocity anomaly is indicative of high temperatures and a small amount of melt and we suggest that it represents the current magma plumbing system for melts ascending from the mantle.

[34] 2. Seismic anisotropy in the lower crust at the segment center indicates that the lower crust is composed of partially molten dikes that are surrounded by regions of hot rock with little to no melt fraction.

[35] 3. At the segment center, mantle level focusing of melt creates a thinner lithosphere and a thicker crust (8.5 km thick versus $< 4\text{--}5$ km at the ends), and results in plate spreading being accommodated more by magmatism than tectonism as compared to the segment ends.

[36] 4. At the segment ends, the lack of magma supply and resultant tectonic stretching opens cracks that allow deep cooling of the crust.

[37] 5. Scattered velocity anomalies and nonuniform aging of the shallow crust indicate that formation of the shallow crust is unstable over time, revealing a strong interplay between magmatism, tectonism, and hydrothermal circulation. In contrast, the relative uniformity of the crust’s thickness as a function of age indicates that the time-averaged melt flux to the ridge is uniform.

[38] 6. Shallow crustal anisotropy is 2–3% with the fast axis aligned with the ridge axis and can be ascribed to dilatational cracks in a stressed lithosphere.

[39] 7. Mantle anisotropy is 3–4% with the azimuth of the fast axis oriented within a few degrees of the predicted direction of ridge migration in the hot spot reference frame. We conclude that mantle strain is not dominated by the direction of relative spreading, but rather the ridge migration direction.

Appendix A

[40] A nonlinear iterative tomographic technique is developed to jointly model marine refraction and reflection travel time data for 3-D velocity structure, layer interface depths, and P wave seismic anisotropy with a hexagonal symmetry system.

A1. Forward Problem

[41] The velocity model for ray tracing is defined on a 3-D grid that includes seafloor topography and is overlain by a water layer [Toomey *et al.*, 1994]. We use a shortest path method, which always finds the global minimum time ray paths in arbitrary media, and is modified to calculate secondary arrivals [Moser, 1991; Klimes and Kvasnicka, 1994]. Ray paths reflected from a structural interface, such as the crust-mantle interface or Moho, are first calculated down to the reflector (the words interface and reflector will be used interchangeably) and then the reflector is used to initialize ray paths that travel upward. Our implementation calculates the paths and times of all portions of the branches of the travel time triplication associated with the interface. The interface is a gridded surface whose x and y (lateral) positions are coincident with the velocity model's x and y positions. The z (depth) positions of the surface vary independently of the z positions of the velocity grid allowing it to vary smoothly. If the interface is raised or lowered, the velocity structure (not the grid itself) is altered to maintain any velocity contrast associated with the interface. For example, if the interface is pushed downward, then crustal values are continued downward to fill the “gap”, which erases the previous mantle values at those grid points.

[42] Seismic anisotropy is often detected in marine seismic data as an azimuthal variation in travel times [e.g., Hess, 1964; Raitt *et al.*, 1969; Barclay *et al.*, 1998; Dunn and Toomey, 2001; Dunn *et al.*, 2001]. The form of the anisotropy is assumed to have a hexagonal symmetry system with the symmetry axis constrained to the horizontal plane. Although an orthorhombic form of anisotropy is possible in the upper mantle [e.g., Ismail and Mainprice, 1998], for refraction studies the ray paths travel nearly horizontal in the mantle and thus sample only one planar cut through a slowness surface. Thus distinguishing between hexagonal and orthorhombic systems is not substantive for modeling the travel times. The anisotropy is defined at each grid vertex and can vary in three dimensions. We approximate the anisotropic P wave slowness (slowness in the inverse of the velocity) as

$$u(\mathbf{r}) = \frac{u_{\text{iso}}(\mathbf{r})}{1 + A(\mathbf{r}) \cos[2\theta(\mathbf{r})] + B(\mathbf{r}) \sin[2\theta(\mathbf{r})]}, \quad (\text{A1})$$

where $u_{\text{iso}}(\mathbf{r})$ is the isotropic slowness at location \mathbf{r} , and θ is the azimuth of a ray measured from the horizontal x axis. A and B are scale terms that control the magnitude and

orientation of the fast direction of anisotropy, which are given by $2(A^2 + B^2)^{0.5}$ and $\text{atan}(B/A)/2$, respectively.

[43] For active source experiments designed to image crustal structure on a 0.5–2 km scale [e.g., Dunn *et al.*, 2000; Barclay *et al.*, 1998], a grid spacing of 150–250 m provides sufficient accuracy. Root-mean-square travel time errors are <5 ms for a grid spacing of 200 m in three dimensions and <2 ms for ray tracing in two dimensions, a factor of 10 smaller than other errors commonly associated with marine seismic experiments. In general, the magnitude of the errors depends on the ray path lengths, the velocity values, and the form of the forward star; a forward star is a set of ray path arcs used to search for the minimum time path [Moser, 1991].

A2. Inverse Problem

[44] The travel time along a ray P through a slowness model $u(\mathbf{r})$ is

$$t = \int_P u(\mathbf{r}) ds, \quad (\text{A2})$$

where ds is the incremental path length. A general slowness model is related to the starting model $u_o(\mathbf{r})$ by

$$u(\mathbf{r}) = u_o(\mathbf{r}) + \delta u(\mathbf{r}), \quad (\text{A3})$$

where $\delta u(\mathbf{r})$ is a perturbation to the starting model. Likewise, an interface position is

$$z(\mathbf{r}) = z_o(\mathbf{r}) + \delta z(\mathbf{r}), \quad (\text{A4})$$

where $\delta z(\mathbf{r})$ is a perturbation to the starting position $z_o(\mathbf{r})$. Given a small perturbation δu , Fermat's principle tells us that the first-order change in travel time along the r th path is

$$\delta t_r = \int_{P(u_o)} \delta u ds. \quad (\text{A5})$$

For a ray transmitted either downward or upward across an interface the first-order change in travel time produced by a vertical displacement δz of the interface at the position \mathbf{r}_o where the ray intersects the interface is

$$\delta t_r = [u_1(\mathbf{r}_o) \cos(\eta) - u_2(\mathbf{r}_o) \cos(\omega)] \cos(\xi) \delta z(\mathbf{r}_o); \quad (\text{A6})$$

u_1 and u_2 are the slowness values on either side of the interface, η is the angle between the incident ray and the surface normal, ω is the angle of the transmitted ray with the surface normal, and ξ is the angle between the surface normal and the vertical axis [Sambridge, 1990]. For a reflected ray the expression is

$$\delta t_k = 2u(\mathbf{r}_o) \cos(\eta) \cos(\xi) \delta z(\mathbf{r}_o); \quad (\text{A7})$$

$u(\mathbf{r}_o)$ is the slowness above the reflection point in this case [e.g., Bishop *et al.*, 1985].

[45] The forward and inverse problems are parameterized separately (i.e., the grid spacing is different) for flexibility and computational efficiency. Following Toomey *et al.* [1994], the perturbational model $\delta u(\mathbf{r})$, defined on the finer grid, is given by linear interpolation between pertur-

bation values α_i at a set of coarsely spaced parametric nodes ($i = 1, \dots, m$):

$$\delta u(\mathbf{r}; \alpha_1, \alpha_2, \dots, \alpha_m) = \sum_{i=1}^m w_i(\mathbf{r}) \alpha_i. \quad (\text{A8})$$

The linear interpolation weights, w_i , [e.g., *Thurber, 1983*] are defined locally using only those parametric nodes that are immediately adjacent to the position \mathbf{r} . Therefore, for a 3-D model there are eight nonzero weights. Likewise, $\delta z(\mathbf{r})$ is defined by linear interpolation between values at nodes located on a reflector:

$$\delta z(\mathbf{r}; \beta_1, \beta_2, \dots, \beta_n) = \sum_{j=1}^n w_j(\mathbf{r}) \beta_j. \quad (\text{A9})$$

There are four nonzero weights for a two-dimensional reflection surface. Again for anisotropy:

$$\delta A(\mathbf{r}; \gamma_1^1, \gamma_2^1, \dots, \gamma_o^1) = \sum_{k=1}^o w_k(\mathbf{r}) \gamma_k^1 \quad (\text{A10})$$

$$\delta B(\mathbf{r}; \gamma_1^2, \gamma_2^2, \dots, \gamma_o^2) = \sum_{k=1}^o w_k(\mathbf{r}) \gamma_k^2. \quad (\text{A11})$$

The goal of the inverse problem is to solve for the values of the α s, β s, and $\gamma^{1,2}$ s, which are then mapped onto the fine grid for ray tracing via (A9)–(A11).

[46] The linearized equation that relates changes in the r th travel time to model parameter changes is written as

$$\delta t_r \left(\alpha_1, \dots, \alpha_m; \beta_1, \dots, \beta_n; \gamma_1^{1,2}, \dots, \gamma_o^{1,2} \right) = \sum_{i=1}^m \frac{\partial t_r}{\partial \alpha_i} \alpha_i + \sum_{j=1}^n \frac{\partial t_r}{\partial \beta_j} \beta_j + \sum_{k=1}^o \left(\frac{\partial t_r}{\partial \gamma_k^1} \gamma_k^1 + \frac{\partial t_r}{\partial \gamma_k^2} \gamma_k^2 \right). \quad (\text{A12})$$

Combining (A5), (A8), and the first term on the right-hand side of (A12) and multiplying the result by the Kronecker delta δ_{ni} , provides the partial derivative relating a travel time variation to a change in the n th parameter used to define the isotropic slowness perturbational model:

$$\frac{\partial t_r}{\partial \alpha_n} = \int_P w_n ds. \quad (\text{A13})$$

For rays transmitted across an interface, we combine (A6), (A9), and the second term of (A12) and multiply the result by the Kronecker delta δ_{ni} , and obtain the partial derivative relating a travel time variation to a vertical change in the interface:

$$\frac{\partial t_r}{\partial \beta_n} = [u_1(\mathbf{r}_o) \cos(\eta) - u_2(\mathbf{r}_o) \cos(\omega)] \cos(\xi) w_n. \quad (\text{A14})$$

Similarly, the expression for reflected rays is

$$\frac{\partial t_r}{\partial \beta_n} = 2u(\mathbf{r}_o) \cos(\eta) \cos(\xi) w_n. \quad (\text{A15})$$

Adding anisotropy to the problem changes (A13) to

$$\frac{\partial t_r}{\partial \alpha_n} = \frac{\partial t_r}{\partial \alpha_n} \frac{\partial \alpha'_n}{\partial \alpha_n} = \int_P w_n ds \frac{\partial \alpha'_n}{\partial \alpha_n}, \quad (\text{A16})$$

where

$$\frac{\partial \alpha'}{\partial \alpha} = \frac{1}{1 + A(\mathbf{r}) \cos[2\theta(\mathbf{r})] + B(\mathbf{r}) \sin[2\theta(\mathbf{r})]}; \quad (\text{A17})$$

α' is an anisotropic slowness perturbation and α is an isotropic slowness perturbation. Likewise for either γ^1 or γ^2 ,

$$\frac{\partial t_r}{\partial \gamma_n^{1,2}} = \frac{\partial t_r}{\partial \alpha'_n} \frac{\partial \alpha'_n}{\partial \gamma_n^{1,2}} = \int_P w_n ds \frac{\partial \alpha'_n}{\partial \gamma_n^{1,2}} \quad (\text{A18})$$

$$\frac{\partial \alpha'}{\partial \gamma^{1,2}} = \frac{-u_{iso}(\mathbf{r}) \cos[2\theta(\mathbf{r})]}{\{1 + A(\mathbf{r}) \cos[2\theta(\mathbf{r})] + B \sin[2\theta(\mathbf{r})]\}^2}. \quad (\text{A19})$$

These partial derivatives tend to be stable since the azimuth of a ray path changes little from iteration to iteration and since both the denominator and the isotropic slowness generally vary by less than 10%. The slowness terms in the partials for reflector position ((A14) and (A15)) are anisotropic, but the effect is also <10%.

[47] The solution is a tradeoff between the norm of the travel time residuals and the norm of the model, where the latter is subject to user-adjustable constraints, and can be determined by minimizing an objective function such as

$$s^2 = (\Delta \mathbf{t} - \mathbf{G} \Delta \mathbf{m})^T \mathbf{C}_d^{-1} (\Delta \mathbf{t} - \mathbf{G} \Delta \mathbf{m}) + \Delta \mathbf{m}^T \mathbf{C}_m^{-1} \Delta \mathbf{m}. \quad (\text{A20})$$

The partial derivatives for slowness structure, interface depth, and anisotropy fill the matrix \mathbf{G} , $\Delta \mathbf{t}$ is a vector of the differences between the observed and calculated travel times, and $\Delta \mathbf{m}$ is a vector of model perturbations to be determined (i.e., α s, β s, and $\gamma^{1,2}$ s). \mathbf{C}_d is a diagonal matrix composed of the individual travel time uncertainties, and \mathbf{C}_m contains user-defined constraints on the model parameters. Rather than invert \mathbf{C}_d and \mathbf{C}_m directly, in practice the rows of \mathbf{G} and $\Delta \mathbf{t}$ are weighted by \mathbf{C}_d and we then apply the covariance information in \mathbf{C}_m as additional rows to \mathbf{G} [e.g., *van der Sluis and van der Vorst, 1987*]. The solution is then obtained via the LSQR method of *Paige and Saunders* [1982]. A linear set of equations whose solution satisfies the minimization of (A20) and which applies the model constraints to the total solution [*Shaw and Orcutt, 1985*] is

$$\begin{bmatrix} \mathbf{C}_d^{-1/2} \mathbf{G} \\ \mathbf{C}_p^{-1/2} \\ \mathbf{C}_s \end{bmatrix} [\Delta \mathbf{m}_{i+1}] = \begin{bmatrix} \mathbf{C}_d^{-1/2} \Delta \mathbf{t} \\ -\mathbf{C}_p^{-1/2} \Delta \mathbf{m}_i \\ -\mathbf{C}_s \Delta \mathbf{m}_i \end{bmatrix}. \quad (\text{A21})$$

Here \mathbf{C}_m is separated into \mathbf{C}_p and \mathbf{C}_s . \mathbf{C}_p is a penalty matrix on the model variance:

$$\mathbf{C}_p = \begin{bmatrix} \sigma_{a1}^2 u_{o1}^2 & 0 & \dots & 0 \\ 0 & \ddots & & \\ & \sigma_{am}^2 u_{om}^2 & & \\ & \sigma_{z1}^2 & & \\ & & \ddots & \\ & & \sigma_{zn}^2 & \\ \vdots & & \sigma_{a1}^2 & \vdots \\ & & & \ddots & \\ & & & \sigma_{ao}^2 & \sigma_{a1}^2 \\ 0 & \dots & 0 & \sigma_{ao}^2 \end{bmatrix}, \quad (\text{A22})$$

where σ_{ui} is the prior fractional uncertainty in the i th model parameter for isotropic slowness and u_{oi} is the slowness value of the prior model, u_{os} , at the position of the i th parameter [Toomey *et al.*, 1994]. Normalization of the slowness constraint by the initial model eliminates bias due to large velocity changes with depth in the prior model [Wiggins, 1972]. σ_{zi} is the prior depth uncertainty of the i th reflector parameter. Likewise, σ_{ai} is the prior uncertainty in the values of γ^1 and γ^2 . The σ values act as damping constraints on the magnitude of model changes; in general, all of the σ for a given parameter type are assigned the same value. C_s provides constraints on the smoothness of the slowness, reflector depth, and anisotropy perturbations. For smoothness constraints on slowness structure, see Toomey *et al.* [1994, equations (10) and (11)]. Similar equations are used for the anisotropy and reflector parameters. For example, a smoothness constraint for the i th parameter β_i for reflector topography has the form

$$\lambda_z \beta_i = \frac{\lambda_z \sum_{j=1}^n v_j \beta_j}{\sum_{j=1}^n v_j}, \quad i \neq j, \quad v_j = \exp \left[-\frac{(x_j - x_i)^2}{(\tau_x \Delta x)^2} - \frac{(y_j - y_i)^2}{(\tau_y \Delta y)^2} \right]. \quad (\text{A23})$$

The value (x, y) is the Cartesian coordinates of a perturbation parameter. The values τ_x and τ_y are the spatial smoothing lengths given as a percentage of the grid spacing Δx and Δy . The importance of satisfying the smoothness constraints is user adjustable via weighting values λ_u , λ_z , and λ_a , which scale the values of the smoothing functions (the subscripts indicate slowness, reflector topography, and anisotropy, respectively). The ratios σ_u/σ_z and λ_u/λ_z control the relative importance of fitting the data with slowness perturbations versus interface depth perturbations. Similarly, the ratios σ_u/σ_a and λ_u/λ_a control the importance of fitting the data with slowness versus anisotropy perturbations. The relative importance of refraction versus reflection data is already incorporated in the data covariance matrix C_d .

[48] A rough grid search can be performed by varying the six values σ_u , σ_z , σ_a , λ_u , λ_z , and λ_a to find a range of smooth models that satisfy the data misfit function:

$$\chi^2 = \frac{1}{N} \sum_{i=1}^N \frac{\Delta t_i^2}{\sigma_{d,i}^2} \approx 1, \quad (\text{A24})$$

where N is the number of travel time picks. A χ^2 value of one indicates that the solution satisfies the data within the limits of data uncertainties. Thereafter, hypothesis tests can be constructed to determine the importance of satisfying the data with isotropic velocity perturbations versus interface perturbations or anisotropy.

[49] For the results presented in this paper, we apply the constraint equations to the current iteration only by setting the $\Delta \mathbf{m}_i$ to zero in equation (A21). We found that by applying the constraints to the whole solution, we were unable to find solutions that fit the data within the assigned uncertainties, and significant trends remained in the data, or the solutions fit the data, but the models were significantly corrupted by data noise. We obtained smoother solutions that fit the data by applying the constraints to each iteration

and using larger smoothing weights and smaller model uncertainties. We suggest that this is due to the nonlinear nature of the problem and because the starting 1-D model is far from the final 3-D solutions.

[50] **Acknowledgments.** We thank Andrew Barclay for comments on the manuscript and for providing the FARA data. We also thank Allegra Hosford Scheirer, who extracted the raw data files of the MARBE experiment from the WHOI database and helped with many details related to organizing and processing this data. Two anonymous reviewers provided constructive and thorough reviews of the manuscript. This research was supported by U.S. National Science Foundation grants OCE-0203228 and OCE-0136793; support for V. Lekic was provided by the IRIS undergraduate internship program.

References

- Abelson, M., G. Baer, and A. Agnon (2001), Evidence from gabbro of the Troodos ophiolite for lateral magma transport along a slow spreading mid-ocean ridge, *Nature*, *409*, 72–75.
- Auld, B. A. (1973), *Acoustic Fields and Waves in Solids*, vol. 1, 423 pp., John Wiley, Hoboken, N. J.
- Barclay, A. H., and D. R. Toomey (2003), Shear wave splitting and crustal anisotropy at the Mid-Atlantic Ridge, 35°N, *J. Geophys. Res.*, *108*(B8), 2378, doi:10.1029/2001JB000918.
- Barclay, A. H., D. R. Toomey, and S. C. Solomon (1998), Seismic structure and crustal magmatism at the Mid-Atlantic Ridge, 35°N, *J. Geophys. Res.*, *103*, 17,827–17,844.
- Barclay, A. H., D. R. Toomey, and S. C. Solomon (2001), Microearthquake characteristics and crustal V_p/V_s structure at the Mid-Atlantic Ridge, 35°N, *J. Geophys. Res.*, *106*, 2017–2034.
- Bishop, T. N., K. P. Bube, R. T. Cutler, R. T. Langan, P. L. Love, J. R. Resnick, R. T. Shuey, D. A. Spindler, and H. W. Wyld (1985), Tomographic determination of velocity and depth in laterally varying media, *Geophysics*, *50*, 903–923.
- Canales, J. P., R. S. Detrick, J. Lin, and J. A. Collins (2000a), Crustal and upper mantle seismic structure beneath the rift mountains and across a nontransform offset at the Mid-Atlantic Ridge (35°N), *J. Geophys. Res.*, *105*, 2699–2719.
- Canales, J. P., J. A. Collins, J. Escartin, and R. S. Detrick (2000b), Seismic structure across the rift valley of the Mid-Atlantic Ridge at 23°20'N (MARK area): Implications for crustal accretion processes at slow spreading ridges, *J. Geophys. Res.*, *105*, 28,411–28,425.
- Cannat, M. (1993), Emplacement of mantle rocks in the seafloor at mid-ocean ridges, *J. Geophys. Res.*, *98*, 4163–4172.
- Cannat, M. (1996), How thick is the magmatic crust at slow spreading oceanic ridges?, *J. Geophys. Res.*, *101*, 2847–2857.
- Chin, C., G. P. Klinkhammer, and C. Wilson (1998), Detection of hydrothermal plumes on the northern Mid-Atlantic Ridge: Results from optical measurements, *Earth Planet. Sci. Lett.*, *162*, 1–13.
- DeMets, C., R. G. Gordon, D. F. Argus, and S. Stein (1990), Current plate motions, *Geophys. J. Int.*, *101*, 425–478.
- Detrick, R. S., J. Collins, R. Stephen, and S. Swift (1994), In situ evidence for the nature of the seismic layer 2/3 boundary in oceanic crust, *Nature*, *370*, 288–290.
- Detrick, R. S., H. D. Needham, and V. Renard (1995), Gravity anomalies and crustal thickness variations along the Mid-Atlantic Ridge between 33°N and 40°N, *J. Geophys. Res.*, *100*, 3767–3787.
- Dunn, R. A., and D. R. Toomey (2001), Crack induced seismic anisotropy in the oceanic crust across the East Pacific Rise, *Earth Planet. Sci. Lett.*, *189*, 9–17.
- Dunn, R. A., D. R. Toomey, and S. C. Solomon (2000), Three-dimensional seismic structure and physical properties of the crust and shallow mantle beneath the East Pacific Rise at 9°30'N, *J. Geophys. Res.*, *105*, 23,537–23,555.
- Dunn, R. A., D. R. Toomey, R. S. Detrick, and W. S. D. Wilcock (2001), Continuous mantle melt supply beneath an overlapping spreading center on the East Pacific Rise, *Science*, *291*, 1955–1958.
- Gràcia, E., D. Bideau, R. Hekinian, Y. Lagabrielle, and L. M. Parson (1997), Along-axis magmatic oscillations and exposure of ultramafic rocks in a second-order segment of the Mid-Atlantic Ridge (33°43'N to 24°07'N), *Geology*, *25*, 1059–1062.
- Gràcia, E., D. Bideau, R. Hekinian, and Y. Lagabrielle (1999), Detailed geological mapping of two contrasting second-order segments of the Mid-Atlantic Ridge between Oceanographer and Hayes fracture zones (33°30'N–35°N), *J. Geophys. Res.*, *104*, 22,903–22,921.
- Grevenmeyer, I., and W. Weigel (1997), Increase of seismic velocities in upper oceanic crust: The “superfast” spreading East Pacific Rise at 14°14'S, *Geophys. Res. Lett.*, *24*, 217–220.

- Gripp, A., and R. Gordon (2002), Young tracks of hotspots and current plate velocities, *Geophys. J. Int.*, *150*, 321–361.
- Hess, H. H. (1964), Seismic anisotropy of the uppermost mantle under oceans, *Nature*, *203*, 629–631.
- Hoofft, E. E. E., R. S. Detrick, D. R. Toomey, J. A. Collins, and J. Lin (2000), Crustal thickness and structure along three contrasting spreading segments of the Mid-Atlantic Ridge, 33.5°–35°N, *J. Geophys. Res.*, *105*, 8205–8226.
- Hosford, A., J. Lin, and R. S. Detrick (2001), Crustal evolution over the last 2 m.y. at the Mid-Atlantic Ridge OH-1 segment, 35°N, *J. Geophys. Res.*, *106*, 13,269–13,285.
- Houtz, R., and J. I. Ewing (1976), Upper crustal structure as a function of plate age, *J. Geophys. Res.*, *81*, 2490–2498.
- Hussenöeder, S. A., G. M. Kent, and R. S. Detrick (2002), Upper crustal seismic structure of the slow spreading Mid-Atlantic Ridge, 35°N: Constraints on volcanic emplacement process, *J. Geophys. Res.*, *107*(B8), 2156, doi:10.1029/2001JB001691.
- Ismail, W. B., and D. Mainprice (1998), An olivine fabric database: An overview of upper mantle fabrics and seismic anisotropy, *Tectonophysics*, *296*, 145–157.
- Jousselin, D., R. A. Dunn, and D. R. Toomey (2003), Modeling the seismic signature of structural data from the Oman Ophiolite: Can a mantle diapir be detected beneath the East Pacific Rise?, *Geochem. Geophys. Geosyst.*, *4*(7), 8610, doi:10.1029/2002GC000418.
- Klimes, L., and M. Kvasnicka (1994), 3-D network ray tracing, *Geophys. J. Int.*, *116*, 726–738.
- Kuo, B.-Y., and D. W. Forsyth (1988), Gravity anomalies of the ridge-transform system in the South Atlantic between 31 and 34.5°S: Upwelling centers and variations in crustal thickness, *Mar. Geophys. Res.*, *10*, 205–232.
- Le Douaran, S., H. D. Needham, and J. Francheteau (1982), Pattern of opening rates along the axis of the Mid-Atlantic Ridge, *Nature*, *300*, 254–257.
- Lin, J., and J. Phipps Morgan (1992), The spreading rate dependence of three-dimensional mid-ocean ridge gravity structure, *Geophys. Res. Lett.*, *19*, 13–16.
- Lin, J., G. M. Purdy, H. Schouten, J.-C. Sempere, and C. Zervas (1990), Evidence from gravity data for focused magmatic accretion along the Mid-Atlantic Ridge, *Nature*, *344*, 627–632.
- Magde, L. S., D. W. Sparks, and R. S. Detrick (1997), The relationship between buoyant mantle flow, melt migration, and gravity bull's eyes at the Mid-Atlantic Ridge between 33°N and 35°N, *Earth Planet. Sci. Lett.*, *148*, 59–67.
- Magde, L. S., A. H. Barclay, D. R. Toomey, R. S. Detrick, and J. A. Collins (2000), Crustal magma plumbing within a segment of the Mid-Atlantic Ridge, 35°N, *Earth Planet. Sci. Lett.*, *175*, 55–67.
- Moser, T.-J. (1991), Shortest path calculation of seismic rays, *Geophysics*, *56*, 59–67.
- Niu, Y., D. Bideau, R. Hekinian, and R. Batiza (2001), Mantle compositional control on the extent of mantle melting, crust production, gravity anomaly, ridge morphology, and ridge segmentation, *Earth Planet. Sci. Lett.*, *186*, 383–399.
- Paige, C. C., and M. A. Saunders (1982), LSQR: An algorithm for sparse linear equations and sparse least squares, *Trans. Math. Software*, *8*, 43–71.
- Parsons, L., E. Gràcia, D. Collier, C. German, and D. Needham (2000), Second-order segmentation: The relationship between volcanism and tectonism at the MAR, 38°N–35°40'N, *Earth Planet. Sci. Lett.*, *178*, 231–251.
- Phipps Morgan, J., and Y. J. Chen (1993), The genesis of oceanic crust: Magma injection, hydrothermal circulation, and crustal flow, *J. Geophys. Res.*, *98*, 6283–6298.
- Purdy, G. M. (1987), New observations of the shallow seismic structure of young oceanic crust, *J. Geophys. Res.*, *92*, 9351–9362.
- Purdy, G. M., and R. S. Detrick (1986), Crustal structure of the Mid-Atlantic Ridge at 23°N from seismic refraction studies, *J. Geophys. Res.*, *91*, 3739–3762.
- Rabain, A., M. Cannat, J. Escartín, G. Pouliquen, C. Deplus, and C. Rommevaux-Jestin (2001), Focused volcanism and growth of a slow spreading segment (Mid-Atlantic Ridge, 35°N), *Earth Planet. Sci. Lett.*, *185*, 211–224.
- Rabinowicz, M., S. Rouzo, J.-C. Sempere, and C. Rosemberg (1993), Three-dimensional mantle flow beneath mid-ocean ridges, *J. Geophys. Res.*, *98*, 7851–7869.
- Raitt, R. W., G. G. Shor, T. J. G. Francis, and G. B. Morris (1969), Anisotropy of the Pacific upper mantle, *J. Geophys. Res.*, *74*, 3095–3109.
- Ross, W. S. (1994), The velocity-depth ambiguity in seismic traveltimes data, *Geophysics*, *59*, 830–843.
- Sambridge, M. S. (1990), Non-linear arrival time inversion: Constraining velocity anomalies by seeking smooth models in 3-D, *Geophys. J. Int.*, *102*, 653–677.
- Schmeling, H. (1985), Numerical models on the influence of partial melt on elastic, anelastic and electrical properties of rocks, part I: Elasticity and anelasticity, *Phys. Earth Planet. Inter.*, *41*, 34–57.
- Schoenberg, M. (1983), Reflection of elastic waves from periodically stratified media with interfacial slip, *Geophys. Prospects*, *31*, 265–292.
- Shaw, P., and J. A. Orcutt (1985), Waveform inversion of seismic refraction data and applications to young Pacific crust, *Geophys. J. R. Astron. Soc.*, *82*, 375–414.
- Sinha, M. C., and K. E. Loudon (1983), The Oceanographer fracture zone—I: Crustal structure from seismic refraction studies, *Geophys. J. R. Astron. Soc.*, *75*, 713–736.
- Sinton, J. M., and R. S. Detrick (1992), Mid-ocean ridge magma chambers, *J. Geophys. Res.*, *97*, 197–216.
- Smith, D. K., and J. R. Cann (1999), Constructing the upper crust of the Mid-Atlantic Ridge: A reinterpretation based on the Puna Ridge, Kilauea Volcano, *J. Geophys. Res.*, *104*, 25,379–25,399.
- Sparks, D. W., E. M. Parmentier, and J. Phipps Morgan (1993), Three-dimensional mantle convection beneath a segmented spreading center: Implications for along-axis variations in crustal thickness and gravity, *J. Geophys. Res.*, *98*, 21,977–21,995.
- Spudich, P., and J. A. Orcutt (1980), Petrology and porosity of an oceanic crust site: Results from waveform modeling of seismic refraction data, *J. Geophys. Res.*, *85*, 1409–1433.
- Stein, S., H. J. Melosh, and J. B. Minster (1977), Ridge migration and asymmetric sea-floor spreading, *Earth Planet. Sci. Lett.*, *36*, 51–62.
- Swift, S. A., D. Lizarralde, H. Hoskins, and R. A. Stephen (1998), Velocity structure in the upper ocean crust at Hole 504B from vertical seismic profiles, *J. Geophys. Res.*, *103*, 15,361–15,376.
- Thibaud, R., P. Gente, and M. Maia (1998), A systematic analysis of the Mid-Atlantic Ridge morphology and gravity between 15°N and 40°N: Constraints of thermal structure, *J. Geophys. Res.*, *103*, 24,223–24,243.
- Thurber, C. H. (1983), Earthquake locations and three-dimensional crustal structure in the Coyote Lake area, central California, *J. Geophys. Res.*, *88*, 8226–8236.
- Tolstoy, M., A. J. Harding, and J. A. Orcutt (1993), Crustal thickness on the Mid-Atlantic Ridge: Bull's-eye gravity anomalies and focused accretion, *Science*, *262*, 726–729.
- Toomey, D. R., S. C. Solomon, and G. M. Purdy (1994), Tomographic imaging of the shallow crustal structure of the East Pacific Rise at 9°30'N, *J. Geophys. Res.*, *99*, 24,135–24,157.
- Tucholke, B. E., and J. Lin (1994), A geologic model for the structure of ridge segments in slow spreading ocean crust, *J. Geophys. Res.*, *99*, 11,937–11,958.
- van der Sluis, A., and H. A. van der Vorst (1987), Numerical solutions of large sparse algebraic systems arising from tomographic problems, in *Seismic Tomography*, edited by G. Nolet, pp. 49–83, Springer, New York.
- Whitehead, J. A., Jr., H. J. B. Dick, and H. Schouten (1984), A mechanism for magmatic accretion under spreading centers, *Nature*, *312*, 146–148.
- Wiggins, R. A. (1972), The general linear inverse problem: Implication of surface waves and free oscillations for Earth structure, *Rev. Geophys.*, *10*, 251–285.

R. S. Detrick, Department of Geology and Geophysics, Woods Hole Oceanographic Institution, 360 Woods Hole Road, Woods Hole, MA 02543, USA.

R. A. Dunn, Department of Geology and Geophysics, SOEST, University of Hawai'i at Manoa, 1680 East-West Road, Honolulu, HI 96822, USA. (dunnr@hawaii.edu)

V. Lekić, Department of Earth and Planetary Science, College of Letters and Science, University of California, Berkeley, 307 McCone Hall, Berkeley, CA 94720-4767, USA.

D. R. Toomey, Department of Geological Sciences, University of Oregon, 1272 Geological Sciences, Eugene, OR 97403-1272, USA.